crystals

MDPI

Article

Nanostructured Mn–Ni Powders Produced by High-Energy Ball-Milling for Water Decontamination from RB5 Dye

Wael Ben Mbarek [1], Mohammed Al Harbi [2], Bechir Hammami [2], Mohamed Khitouni [2,3,*], Luisa Escoda [1] and Joan-Josep Suñol [1]

[1] Department of Physics, Campus Montilivi s/n, University of Girona, 17003 Girona, Spain; benmbarek.wael@hotmail.fr (W.B.M.); joanjosep.sunyol@udg.edu (J.-J.S.)
[2] Department of Chemistry, College of Science, Qassim University, Buraydah 51452, Saudi Arabia; 421100416@qu.edu.sa (M.A.H.); b.hammami@qu.edu.sa (B.H.)
[3] Laboratory Inorganic Chemistry, UR-11-ES-73, Faculty of Science of de Sfax, University of Sfax, B.P. 1171, Sfax 3000, Tunisia
* Correspondence: kh.mohamed@qu.edu.sa; Tel.: +966-55-343-3072

Abstract: In this study, the degradation efficiency of Mn-20at%Ni and Mn-30at%Ni particle powders made by melt-spinning and high-energy ball-milling techniques is investigated in relation to the degradation of the azo dye Reactive Black 5. SEM, EDS, and XRD were used to analyze the powders' morphology, surface elemental composition, and phase structure. An ultraviolet-visible absorption spectrophotometer was used to measure the ball-milled powder's capacity to degrade, and the collected powders were examined using the FTIR spectroscopy method to identify the substituents in the extract. The impact of MnNi alloy on the azo dye Reactive Black 5′s degradation and its effectiveness as a decolorizing agent were examined as functions of different parameters such as chemical composition, specific surface, and temperature. In comparison to the Mn-30at%Ni alloy, the powdered Mn-20at%Ni particles show better degrading efficiency and a faster rate of reaction. This remarkable efficiency is explained by the configuration of the valence electrons, which promotes more responding sites in the d-band when the Ni content is reduced. Therefore, increased electron transport and a hastened decolorization process are achieved by reducing the Ni concentration of RB5 solution with Mn80 particle powder. Additionally, this difference in their decolorization efficiency is explained by the fact that Mn-20at%Ni has the highest specific surface area of 0.45 m^2 g^{-1}. As the main result, the functional uses of nanostructured metallic powder particles as organic pollution decolorizers in the textile industry are greatly expanded by our study.

Keywords: nanomaterials; ball-milling; melt-spinning; decolorization; RB 5; XRD; UV-visible

Citation: Mbarek, W.B.; Al Harbi, M.; Hammami, B.; Khitouni, M.; Escoda, L.; Suñol, J.-J. Nanostructured Mn–Ni Powders Produced by High-Energy Ball-Milling for Water Decontamination from RB5 Dye. *Crystals* **2023**, *13*, 879. https://doi.org/10.3390/cryst13060879

Academic Editor: Nabeen K Shrestha

Received: 9 May 2023
Revised: 18 May 2023
Accepted: 25 May 2023
Published: 27 May 2023

1. Introduction

Due to their high toxicity and slow biodegradation rate, colored effluents have attracted a lot of attention [1–4]. Significant sources of contamination come from the textile industries' dye effluents [5]. Additionally, the textile industry consumes a significant amount of water and generates a lot of wastewater that contains dyes. Because it poses a major problem for sewage treatment stations, the appropriate regeneration of wastewater containing dyes in high quantities is necessary and critical work. Researchers have suggested a number of physicochemical and biological procedures and materials for the treatment of wastewater, including adsorption methods, biodegradation, the coagulation–flocculation method, advanced oxidation, and hypochlorite treatment, ozonation, and hypochlorite treatment [6–9]. The bulk of these processes, however, have limitations. For instance, Fenton, photocatalysts, and other oxidation procedures are highly expensive; biological processes require a long time; and occultation and adsorption may not be successful. Furthermore, it is beneficial to proceed with the cheapest, most accessible, most efficient techniques and materials when degrading azo dyes. One such practical method

is reduction with zero-valent metals (ZVM) such as Mg, Ni, Fe, Zn, Co, or Al, and alloys, which have been investigated as attractive and advantageous routes due to their inexpensive cost merits, rapid degradation performance, and easy operation in the removal of azo dyes [10–18]. Specifically, the degradation reaction was determined by a redox reaction, wherein the surface metal loses electrons to break the active bonds (–N = N–) of the reactive dyes. In contrast to the bulk material, the fine powder form of metals and alloys offers more active surface sites for the reactive degradation of organic compounds. In particular, nanomaterials made up of inorganic components such as semiconductors, metal oxides, and nanocatalysts have attracted a lot of interest as wastewater treatment materials. A range of nanocatalysts are utilized in wastewater treatment, including photocatalysts [19,20], electrocatalysts [19], heterojunction photocatalytic materials [21], and Fenton-based catalysts [22] for analysis of their oxidation of organic contaminants [23] and of their antimicrobial effects [24]. The importance of nanoparticle photocatalytic processes, which are based on the interaction of light energy with metallic nanoparticles, may be seen in their extensive and effective photocatalytic activity on a variety of pollutants. These photocatalysts, which are often composed of semiconductor metals, can break down a range of persistent organic pollutants found in wastewater, such as dyes, detergents, pesticides, and volatile organic compounds [25]. Furthermore, halogenated and non-halogenated organic molecules, as well as many pharmaceuticals, personal care products, and heavy metals, can all be broken down very effectively by semiconductor nanocatalysts [26]. Semiconductor nanomaterials operate under reasonably benign conditions, and perform well even at low concentrations. The photoexcitation of an electron inside the catalyst is the fundamental idea behind how photocatalysis works. When TiO2 is exposed to light (in this case, UV), holes (h+) and ejected electrons (e–) are generated in the conduction band. Water molecules (H2O) absorb holes (h+) in an aqueous solution to create hydroxyl radicals (OH) [27]. The radicals have a potent and indiscriminate oxidizing effect. These hydroxyl radicals convert the organic pollutants into water and gaseous breakdown products [28]. On the other hand, it was discovered that the size, appropriate surface area, shapes, and roughness of nanocrystalline powders had a significant impact on their catalytic activity [29–33]. The use of mechanical alloying in high-energy ball mills is a simple and less complicated technique for producing fine metallic powder particles for decolorizing applications [29,30,34–37]. This is because these ball-milled particles frequently exhibit fine particles with rough surfaces and highly metastable nanocrystalline or amorphous morphologies. Indeed, milled powders undergo severe plastic deformation during this procedure to cause fracture and cold welding, which allows the grains to be refined to a steady state size (50 nm) for the majority of metals and alloys [38–40]. Repetitive fractures and cold welding of the powder particles cause interactions between the initial mixture's solid constituents. As a result of internal strains driven by a high density of dislocations and an important proportion of grain boundaries, mechanically stored enthalpy can act as a catalyst for the creation of nanocrystalline and/or amorphous structures [34,41], helping to enhance the material's mechanical, physical, and magnetic properties [42]. Recently, our research [29,30,35–37] reported on the remarkable effectiveness of mechanically alloyed Mn(Al), Ca(Al), Mn(Al,Co), and Mn(Al,Fe) powder particles in the degradation of azo dyes. In this study, new findings examining various Mn–Ni particle properties will be presented and evaluated against current studies, including the impact of composition and structure on the decomposition rate of RB5. To achieve this, we employ the method of melt spinning succeeded by ball-milling to produce Mn–Ni powder particles with a high surface area, which will increase the efficiency of dye molecule degradation.

2. Materials and Methods

The alloy ingots were made by arc melting a combination of Mn (99.9 wt%) and Ni (99.99 wt%) in a Ti-gettered argon environment to yield alloys with nominal compositions of Mn-30at%Ni and Mn-20at%Ni (at%) alloys. This bulk was heated by induction, melted, and then loaded into a spinning copper wheel through a nozzle that is 0.8 mm wide, producing

40 mm thick, rapidly quenched ribbons. Then, under an Ar atmosphere, the ribbon samples were placed in a ball-milling jar. The samples were milled in an inverse rotational direction, and the ball-milling speed for the jar was 500 rpm. In order to prevent the heat of the sample, powder agglomeration, and adhering to the jar walls and balls, a time of 5 min waiting period was used after each 10 min of milling. There were 15 h spent milling in total. The shape of the ball-milled (BM) powder was examined using scanning electron microscopy (SEM) in a DSM960A ZEISS microscope in secondary electron mode at a voltage of 15 kV. The SEM is equipped with a Vega Tescan energy dispersive X-ray spectrometry (EDS) analyzer. EDX was used to examine the semi-quantitative elemental composition.

Using Micromeritics ASAP 2020 M equipment, the Brunauer, Emmett, and Teller (BET) theory-based gas multilayer adsorption process was employed to determine the specific surface area of the MnNi powder. The observations were made in a nitrogen atmosphere after the powder had been degassed for 24 h at 300 °C.

By employing CuKα radiation with a Siemens D500 powder diffractometer at room temperature, the structural alterations of the milled powders were identified. A full pattern XRD Rietveld fitting approach was used to extract the microstructural properties.

A solution of RB5 with a concentration of 40 mg L^{-1} was employed to assess the colorant degradation process. 100 mL of solution was mixed with 0.25 g of ball-milled powder for each degradation experiment. On a Rotanta 460 r centrifuge, the solution samples were taken at periodic intervals and centrifuged for 15 min at 3000 rpm. An ultraviolet-visible absorption spectrophotometer (UV-Vis) was used to separate the supernatants and measure the color at the RB5 dye's maximum absorption wavelength (Shimadzu 2600 UV-visible). To identify the presence of the substituents in the extract, the powder was examined using a Fourier transform infrared spectroscopy (FTIR) spectrum. The same amount of ground sample was used to make the pellets in each example, and the spectra were calibrated to enable comparisons across various samples.

3. Results

The surface appearance of the BM Mn-30at%Ni (Figure 1(a1,a2)) and Mn-20at%Ni (Figure 1(b1,b2)) powder particles is shown in Figure 1, before they are used to degrade Reactive Black 5. As demonstrated, the severe plastic deformation imparted to the ribbons during the ball-milling process caused the nanostructured powder particles to be discovered to be irregular and/or spherical in shape, with corrugated surfaces. The average particle sizes of Mn-30at%Ni and Mn-20at%Ni alloys, respectively, are determined to be around 14 and 22 μm, showing a very uniform distribution (Figure 2(a2,b2)). The Mn-30at%Ni alloy was revealed to have an average particle size of 14 μm, which is somewhat smaller than the industry average. This small discrepancy can be attributed to the manual selection method of particle powder used for the SEM examination, and the standard error is 8 μm.

The EDS microanalysis shown in Figure 2(a1,b1) demonstrates that the BM powder is mostly made up of the basic elements Mn and Ni, and that there is no contamination from the milling tools or the oxygen in the air. The sputtering procedure that was utilized to prepare the samples for SEM observation is what caused the carbon that was discovered. Mn and Ni, respectively, have contents of 69.68:30.32 and 81.08:18.92 for Mn-30at%Ni and Mn-20at%Ni. These ratios, 70:30 and 80:20, are extremely similar to the nominal composition (Figure 2(a1,b1)).

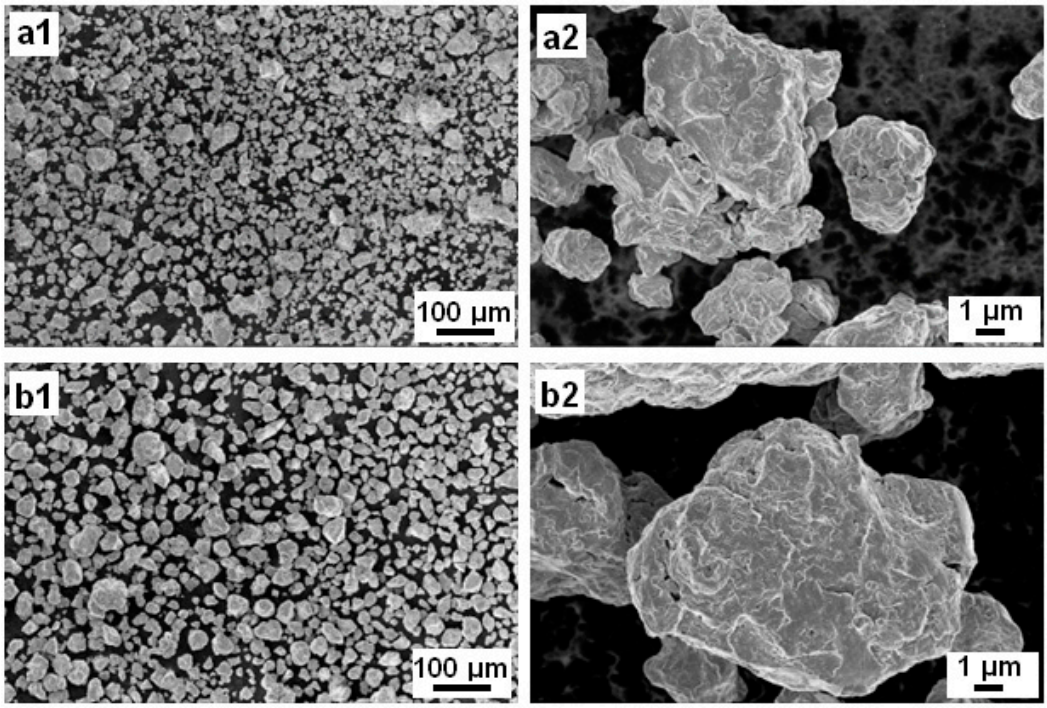

Figure 1. Particle morphologies of the mechanical alloying (MA) Mn-30at%Ni (**a1**,**a2**) and Mn-20at%Ni (**b1**,**b2**) powders (Before degradation).

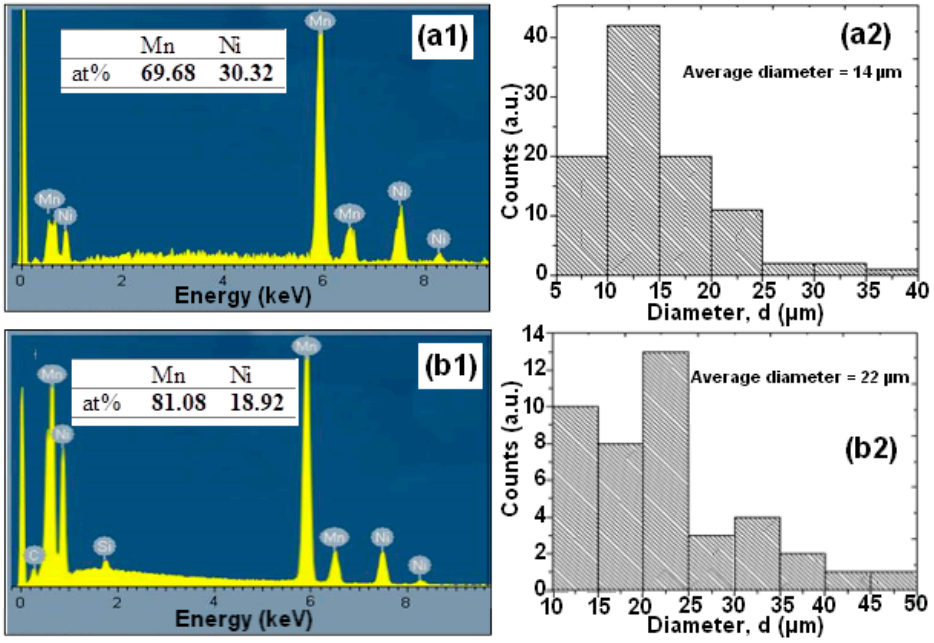

Figure 2. Nominal compositions as examined by EDX and the distribution of particle sizes of the mechanical alloying (MA) Mn-30at%Ni (**a1**,**a2**) and Mn-20at%Ni (**b1**,**b2**) powders (before degradation).

The two binary BM powders, Mn-30at%Ni and Mn-20at%Ni, were used to treat RB5 solutions, and Figure 3a shows representative photographs of these treatments. As shown on the test tubes, the supernatants of both aqueous solutions were separated at 0, 2, 5, 10, 13, 16, 17, and 18 h, as well as 0, 2, 5, and 15 h. It is obvious that both of the RB5 aqueous solutions have undergone decolorization. Figure 3b,c show the matching UV-Vis spectrum variations for both alloy compositions as a function of specified reaction time. The "–N = N–" azo produces the maximum absorbance at max = 597 nm in the visible

area for the time t = 0 h (before treatment by BM powders) [29,35,36,43]. According to previous studies, the relationship between the intensity of this peak and the solution's azo dye content is linear [43,44]. The dye's benzene and naphthalene rings, respectively, are associated with the other two bands in the UV area, which are located at 310 and 230 nm [45,46]. The degradation and evolution of the RB5 chromophores are indicated by the decrease in intensity at 597 nm. In other words, this reduction provides details regarding the azo band cleavage, the creation of ($-NH_2$) groups, and consequently, the breakdown of RB5 in solution. The intensification of the absorbance peak at 267 nm served as additional evidence of the azo band cleavage. The same outcomes have been reported in our most recent research [29,36] when Black 5 dye solutions were reductively degraded by Ca-35at%Al and Mn-15at%Al nanostructured powders. Three hours before the binary Mn-30at%Ni effect on RB5 discoloration, the binary Mn-20at%Ni causes the solution to become completely discolored in 15 h (Figure 3d). However, it appears that when employing the two Mn–Ni powder compositions, the efficiencies of the RB5 decolorization at the same dosage and temperature are different. However, when the Ni content rises and the Mn content falls in the alloy's composition, the question of why there is a 3 h delay in the kinetics of decolorization arises. As was discovered in this work, the same dye solution and Reactive Black 5 dye were decolored using Mn–Ni particle powders with various Mn and Ni contents under the same conditions (milling time, temperature, etc.). The mass transfer effects on the degradation method can be removed as a result. Mn and Ni are both transition metals that make up the alloy's component and have nearly full or partially filled 3d bands. Therefore, it is reasonable to assume that the relative contents of Mn and Ni are responsible for the variances in their decolorization capabilities. In other words, the varied decolorization qualities of Mn–Ni with varying Ni levels depend on the variable Mn and Ni characteristics. The adsorbate in the solution during the decolorization process is the same for both types of nanostructured powders; therefore, the Mn-Ni alloy's electronic structure mostly affects the adsorption of dyes. The van der Waals forces, charge density effect, and transfer forces between the alloys and dye molecules are comparable due to the identical physical characteristics of these nanostructured powders. Therefore, the primary topic of our discussion is covalent or localized bonding. All atoms share the valence electrons of metallic atoms to create an electron cloud with a significantly distributed status, based on the energy band theory [47,48]. The valence electron configurations of Mn and Ni are $4s^2 3d^5$ and $4s^2 3d^8$, respectively. According to magnetic measurements, each atom of Mn and Ni had an average of 1.22 and 0.6 holes in the d band, respectively [48,49]. More unpaired electrons are present when there are more holes. More unpaired electrons correlate to a higher adsorption capacity because the latter can establish a localized adsorption bond with the adsorbate molecules [50,51]. Because Mn80 particle powders have more d band holes per unit of an atom than Mn70 ribbons, they exhibit the highest adsorption efficiency during the first 15 h of the decolorization procedure. However, it is important to keep in mind that these variations could be explained by the varied reduction potentials of Mn and Ni, as well as the various solubilities of respective hydroxides. Given that Mn and Ni are the same components in both alloys, it appears that these differences are related to their elemental composition. The standard oxidation potential of Mn/Mn^{2+} (1.18 V) is more negative than that of Ni/Ni^{2+} (0.23 V), yet it is less negative than that of H^+/H_2 (0.00 V). As a result, the transfer of electrons from Ni to H^+ takes longer than it does from Mn to H^+. According to these hypotheses, decreasing the Ni concentration of RB5 solution with Mn80 particles powder results in improved electron transport and a faster decolorization process. Similar results were found in our most recent work [29], where it was shown that the Mn–Al–Fe powder decolorization reaction occurred more rapidly than the MnAlCo mixture. The different oxidation potentials of Fe/Fe^{2+} (0.44 V) and Co/Co^{2+} (0.34 V) were used to explain this result. Additionally, the rapid decolorization of acid orange II solution is primarily dependent on the amount of Fe present in the Fe–Co–Si–B ribbons [50]. Due to the fact that Fe has a lower oxidation potential than Co, there is a greater electron transfer between Fe and H^+ compared to Co and H^+.

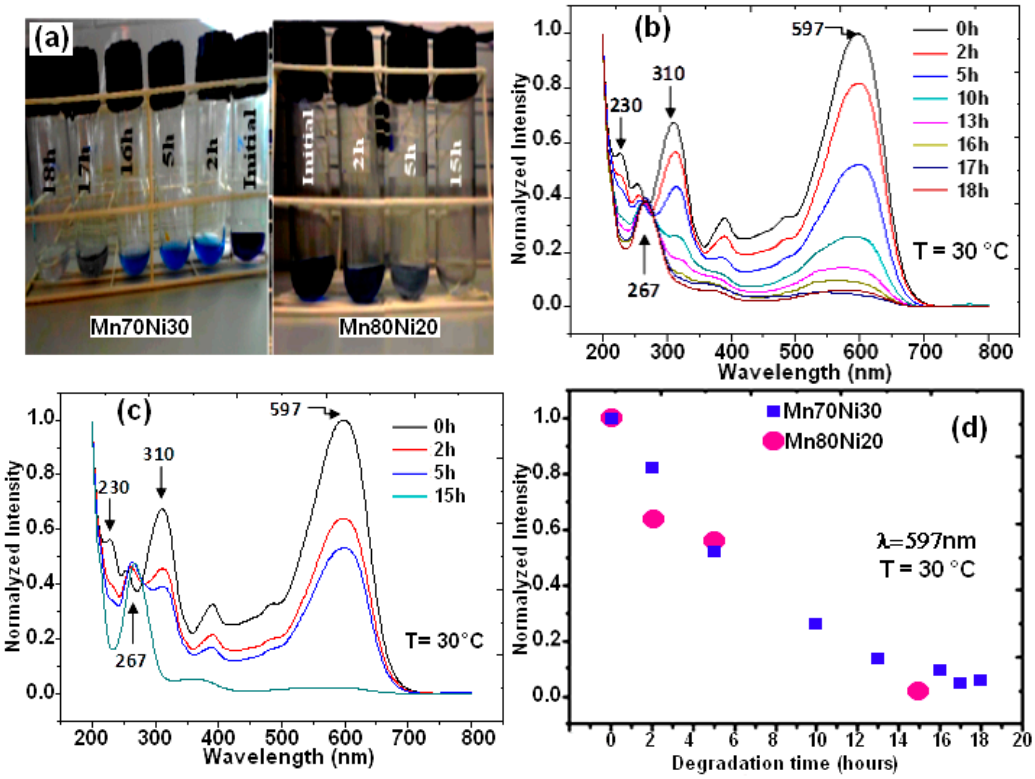

Figure 3. Image of Black 5 solutions processed by MA powders before and after degradation (**a**), UV absorption spectra at different times for Mn-30at%Ni (**b**) and Mn-20at%Ni (**c**) alloys, and the decolorization % from UV absorption intensity at 597 nm versus reaction time for both alloys (**d**).

Four experiments were conducted at temperatures of 25, 30, 40, and 50 °C to track the influence of temperature on the efficiency of the decolorization effect on the degradation of RB5. The exponential function fits the degradation behavior, as seen in Equation (1) [49]:

$$I = I_0 + I_1 e^{-t/t_0} \quad (1)$$

where I is the standardized intensity of the absorption peak, I_0 and I_1 are fitting constants, t is the decolorization time, and t_0 is the moment when the intensity drops to e^{-1} of the original condition; this was calculated by fitting the data points.

The Arrhenius-type Equation (2) can be used to determine the thermal activation energy limit ΔE if we assume that the process is thermally activated:

$$t_0 = \tau_0 - e^{-E/RT} \quad (2)$$

where R is the gas constant and τ_0 is a time pre-factor. Using BM $Mn_{80}Ni_{20}$ powder and a temperature range of 25–50 °C, Figure 4b shows the Arrhenius curve of $\ln(t_0)$ as a function of *1/T* for the decomposition processes of azo dye.

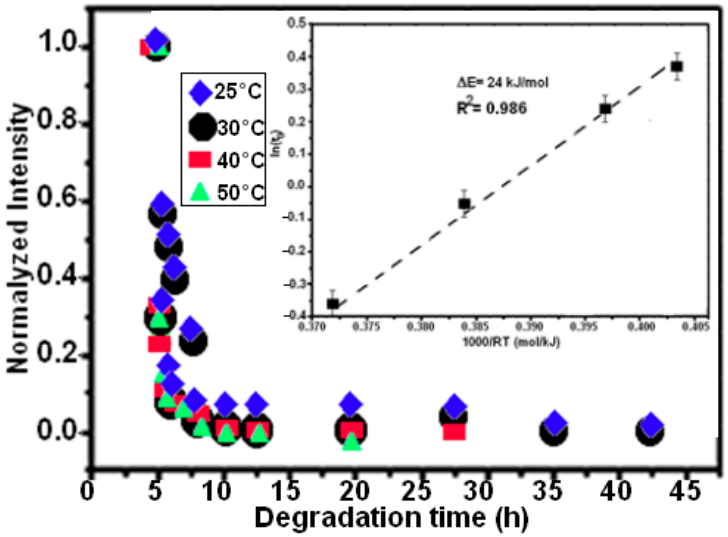

Figure 4. The plot of the decay time (t_0) against temperature and the standardized UV-vis absorption intensity at 597 nm for the MA Mn-20at%Al powder at various temperatures. The fitting of the Arrhenius-type equation to generate the activation energy is represented by the solid lines.

As a result, 24 ± 5 kJ mol^{-1} is the expected ΔE value. The complete degrading reaction took place in 7.5 h, maintaining the extremely high efficiency observed at a temperature of 50 °C. It has previously been noted that activation energy values range between 30 and 80 kJ mol^{-1} for the decolorizing processes of several azo-colorants using metallic particles [31,32,51]. The activation energy for binary $Mn_{85}Al_{15}$ was determined to be 14 kJ mol^{-1} in our recent work on the degradation of RB5 [35]. According to Aboli-Ghasemabadi et al., the activation energy for the MnAl-based degradation of Orange II was 49 ± 5 kJ mol^{-1}. For the heterogeneous decomposition of Orange II with peroxymonosulfate accelerated by mesoporous $MnFe_2O_4$, Deng et al. obtained a value of ΔE = 27.7 kJ mol^{-1} [52]. The activation energy for typical thermal processes is commonly between 60 and 250 kJ mol^{-1}, according to Cheng et al. [53]. In practice, it is impossible to compare the reaction rate to those reported using other materials because of the various utilized conditions, particle weight/solution volume fractions, and type forms of dyes or starting concentrations. The specific surface area of powdered particle components is another concept that can affect the effectiveness of a reaction. The small specific surface area of the powder particles can be used to explain the low reaction efficiency of the ball-milled $Mn_{80}Ni_{20}$ (15 h/30 °C and 7.5 h/50 °C) powder in the current investigation. It is well known that all catalysts preserve a significant amount of surface area [54,55]. The BET method yielded specific surface areas of 0.32 and 0.45 m^2 g^{-1} for Mn-30at%Ni (b) and Mn-20at%Ni, respectively. During the experiment process, the pH values of the solution vary from acid (pH~6 at the beginning of the reaction) to alkaline (pH~9 at the end of the reaction) character. The initial acid behavior around a pH of 6 is due to the solution of the dye. When the reduction reaction takes place, aromatic amines are generated with an increase in pH of around 9. This indicates that the process generates bases that increase the pH. These findings lead us to the conclusion that the redox processes in acidic and alkaline solutions may be related to the phenomenon of degradation. One possible explanation is that as a consequence of the redox process, the protons of the aqueous medium together with the hydrogen atoms cause the generation of hydrogen gas adhered to the metallic surface, and it is the latter that reacts with the azo group, generating aromatic amines. The proposed mechanisms in basic and acidic media, however, were recapped in Table 1. For acid or neutral conditions, the presence of H_3O^+ on the metal surface can facilitate the reduction process, acting as an intermediary in the overall process. The active H2 will reduce the adsorbed azo dye molecules, thereby increasing the decomposition efficiency [35]. Using metallic compositions or ZVM as oxidants, several authors have investigated the effects of an acid medium on the reduction of "–N =

N–" bonds [31,56,57]. They claimed that in an acid media, 100% of the azo dye solution was degraded (an expected result, because in acidic conditions, insoluble hydroxides that prevent the closure of the circuit generated for the electron mobility are not formed).

Table 1. The proposed mechanisms of the degradation process of RB5 in acid or neutral mediums.

The Mechanism in Acid or Neutral Medium	Micropile
$Mn \rightarrow Mn^{2+} + 2e^-$ $H_2O \rightarrow H_3O^+ + OH^-$ $2H_3O^+ + 2e^- \rightarrow H_2 + 2H_2O$ $Mn^{2+} + 2OH^- \rightarrow Mn(OH)_2\downarrow$ $R–N = N–R' + H_2 \rightarrow R–NH–NH–R'$ $R–NH–NH–R' + H_2 \rightarrow R–NH_2 + R'–NH_2$	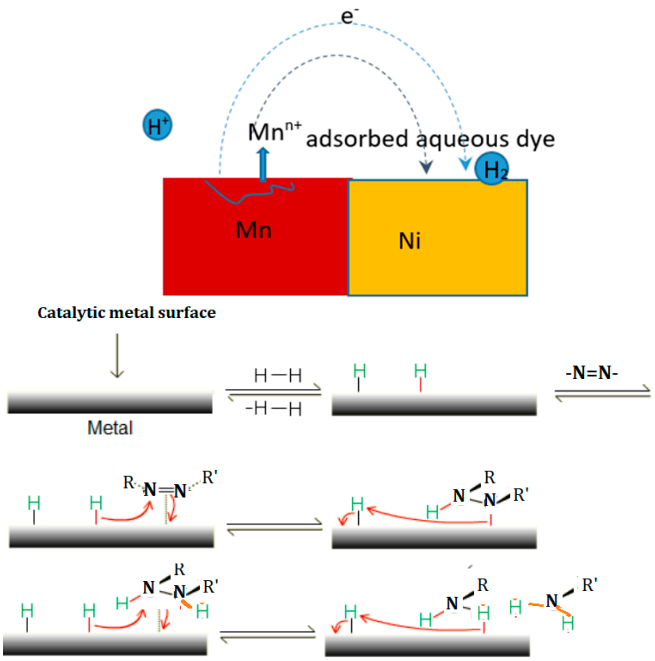

SEM analysis is utilized to describe the powder particle surfaces that were produced after the degradation process. In Figure 5(a1,a2), micrographs of ball-milled $Mn_{70}Al_{30}$ particles show that some reaction products, such as flowered and nanobristles forms, are uniformly adsorbed over the entire surface of the particles. In contrast, in Figure 5(b1,b2), micrographs of $Mn_{80}Ni_{20}$ particles show that nanorods are uniformly distributed on all of the particles' surfaces. Mn_2NiO_4 oxide makes up the majority of these nanorods. Numerous corrosion pits were seen on the surface of the alloy for both particle powders, proving that pitting corrosion on the alloy particles occurred throughout the RB5 degradation process [9,35,58,59]. The related EDS studies shown in Figure 5(a3,b3) reveal the approximate elemental compositions as follows: Mn: 56.63/Ni: 10.58/O: 33.06 for the $Mn_{80}Ni_{20}$ alloy, and Mn: 40.51/Ni: 30.08/O: 29.41 for the $Mn_{80}Ni_{20}$ alloy.

On the other hand, XRD was used to analyze changes in the microstructure of the $Mn_{70}Ni_{30}$ and $Mn_{80}Ni_{20}$ alloys that were noticed after the degradation of RB5. Figure 6 displays the results that were attained. A closer look at the XRD diffractograms of the BM $Mn_{70}Ni_{30}$ and $Mn_{80}Ni_{20}$ powders, which were obtained before the degradation of RB5, reveals that the MnNi phase is primarily present. Ball-milled $Mn_{70}Ni_{30}$ and $Mn_{80}Ni_{20}$ powders have average crystallite diameters of 18 ± 5 nm and 12 ± 5 nm, respectively. By increasing the number of atoms in the boundary regions, this nanocrystalline structure may also contribute to an increase in the reactivity of the powdered $Mn_{80}Ni_{20}$ particles within the aqueous-colored solutions. After degradation, for both powders, we note the appearance of newly identified $Mn_2Ni_1O_4$ oxide (JCPD 98-017-4001), and the $Mn(OH)_2$ (JCPD 00-008-0171), and $Ni(OH)_2$ (JCPD 00-014-0117) hydroxides beside the Mn(Ni) phase (JCPD 98-010-4918) (Figure 6a,b). The new products resemble micro-precipitates covering the surface of the particle powders.

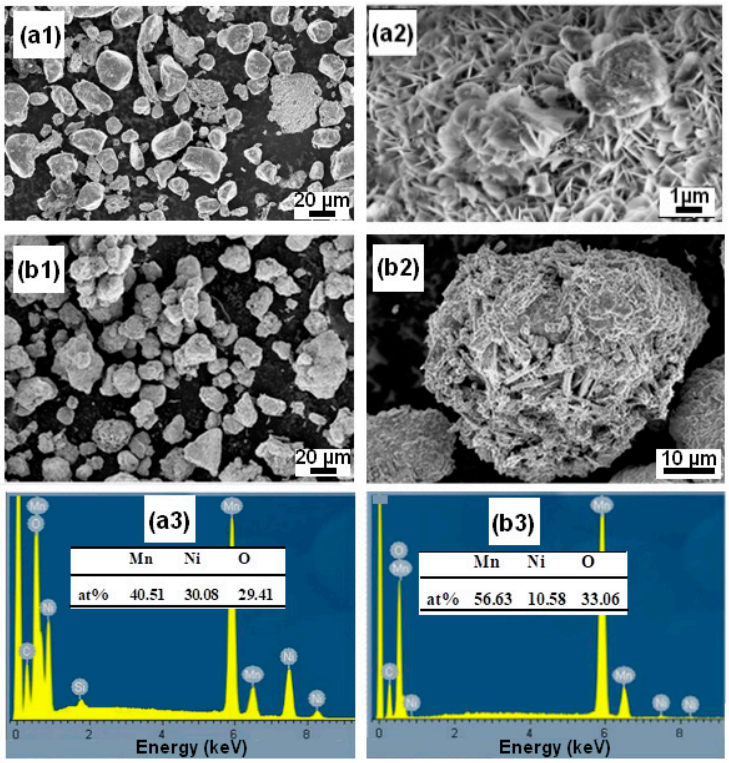

Figure 5. Surface morphologies of the Mn-30at%Ni (**a1**,**a2**) and Mn-20at%Ni (**b1**,**b2**) particle powders, respectively, collected after RB5 decomposition, and their nominal contents as determined by EDX (**a3**,**b3**).

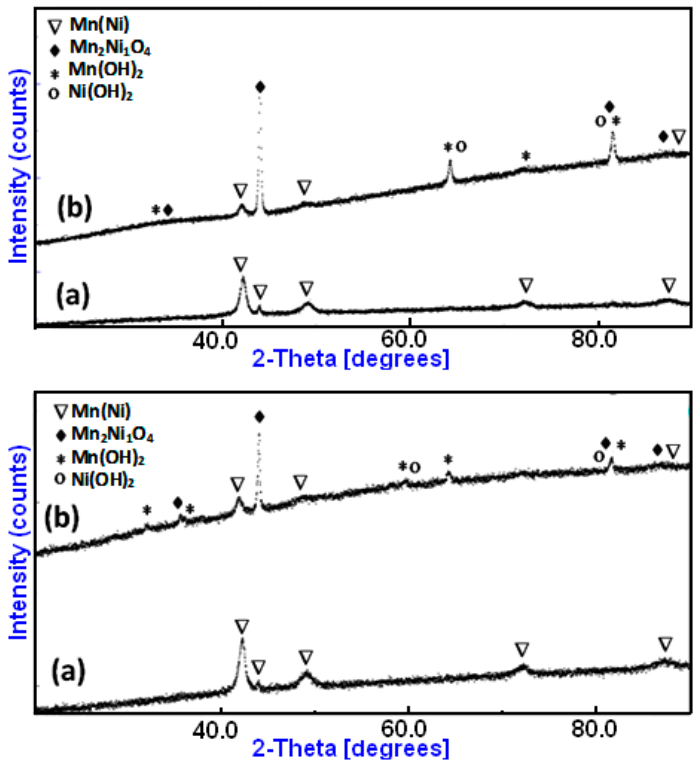

Figure 6. XRD diffraction patterns of MA Mn-30at%Ni (**a**) and Mn-20at%Ni (**b**) powders before and after degradation, respectively.

The FTIR spectrums of $Mn_{70}Ni_{30}$ and $Mn_{80}Ni_{20}$ powders obtained after the degradation reaction of RB5 compared to the initial RB5 powder are given in Figure 7. The FTIR spectrum of RB5 dye before degradation (Figure 7a) showed bands at 3411 cm^{-1}: O-H stretching; 2961 cm^{-1}: skeletal vibration of the benzene ring; 2354 cm^{-1}: aldehyde C-H vibration; 1745 cm^{-1}: C = C stretching vibration; 1635 cm^{-1}: azo bond (–N = N–); 1492 cm^{-1}: C = C aromatic skeletal vibrations; 1186 cm^{-1}: C-OH stretching vibration; 1045 cm^{-1}: C–OH stretching vibration; 1025 cm^{-1}: benzene mode coupling with stretching vibration of $–SO_3$; 805 cm^{-1}: $–CH_3$ skeletal vibration; 616 cm^{-1}: Sulfonic group. All bands are identified on the basis of pieces of information from previous works that studied the degradation of RB5 molecule [60–63] given in Table 2. The availability of active functional groups and the surface characteristics of the biosorbents after interaction with the dye are changes that are evident in the FTIR spectra of both powders after degradation. Some classic RB5 bonds degrade during the degradation, while new bonds arise. Bonds of the naphthalene ring's C = C aromatic skeletal vibration at 1400–1600 cm^{-1} and the azo bond's –N = N– peak at 1635 cm^{-1} are both clearly diminished. All FTIR spectra still contain the 2961 cm^{-1} peak, which is a small peak attributed to the skeletal vibration of the benzene ring. After degradation, a few additional peaks at 1750, 1520, and 1480 cm^{-1} that represent the stretching vibrations of the C = C, N–H, and C–N bonds, respectively, appear (Figure 7a,b). This proves that the existence of amines is promoted by the reductive dissociation of the –N = N bond [29,35,64]. Since amines are recognized to be water pollutants, using Mn-Ni powders in industrial processes must be carried out in combination with an additional amine adsorption procedure. In their recent work, Ben Mbarek and al. [65] were able to effectively remove unwanted intermediate chemicals from reduction processes, mainly aromatic amines. A variety of adsorbents were used, including wood, graphene oxide, activated carbon, and fine particles. These new results indicated that graphene oxide and activated carbon are the best secondary product adsorbents. Indeed, the regeneration of metal powders, synthesized by high-energy mechanosynthesis, and wastewater from discoloration, can serve as a reference for environmental applications in the purification of industrial effluents. On the other hand, the surface of the metals is covered by remnants of adhered dye and by the layer of oxides and/or hydroxides preventing the reaction between the active metal element of the alloy and the H+ of the aqueous solution. The hydrogen produced would be responsible for the attack of the azo group and its reduction in accordance with the mechanism proposed in the work. However, the reduction of the azo group could occur through the direct reaction of the attached dye and Mn, which is the active reducing agent. The oxide layers of both Mn and Ni are more soluble in acidic conditions. A system for removing these oxides would be washing with an acid solution and subsequent removal by rinsing with water. Then, the dry product is rubbed and the action is repeated. Once finished, the powders are dried at room temperature, or ventilation is used to remove the water from the washing. Therefore, maximum regeneration and use of metal powder particles may be implemented to reduce the costs associated with their use, or as possible solutions to minimize material modifications.

The effectiveness of materials used in the removal of organic pollutants depends on the chemical composition in addition to other factors. The first influences both the adsorption and reduction mechanism as well as the kinetics of the reaction. It is difficult to compare bimetallic reducing agents given that having the same composition but a different morphology or structure can produce different efficiencies. Another factor is the pH; the pH directly influences the redox process and the formation of precipitates. Table 3 gives an approximate comparison of the efficiency of the present Mn-Ni powders used in the removal of RB5 organic pollutants to some nanoreductives applied and reported in the previous literature.

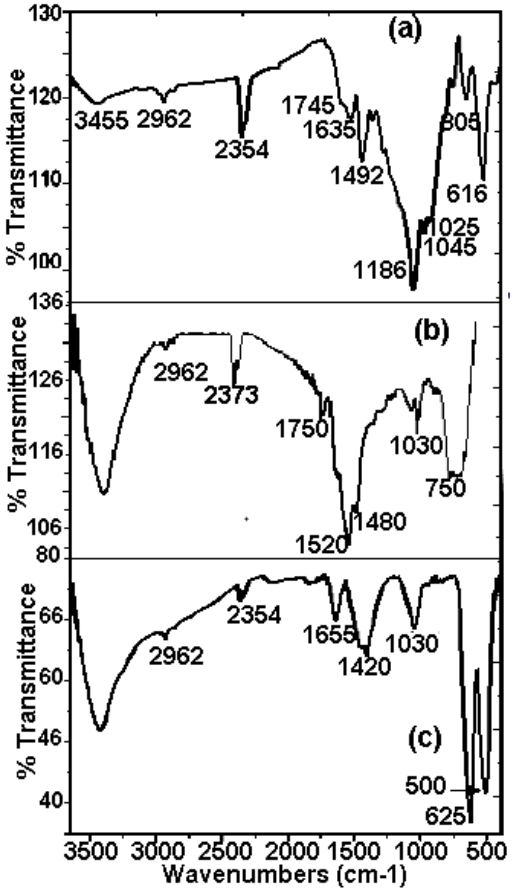

Figure 7. FTIR spectrum of (**a**) RB5 powder before decomposition, and (**b**,**c**) powders Mn-30at%Ni and Mn-20at%Ni, respectively, after decomposition.

Table 2. FTIR bonds identification for RB5 [45–48].

Reactive Black 5 Molecule (M.W.: 991)

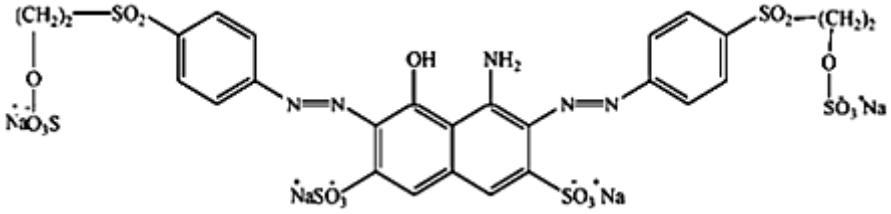

Peak/Band	Identification
3411 cm^{-1}	O–H stretching vibration
2936 cm^{-1}	Benzene ring skeletal vibration
2354 cm^{-1}	C–H aldehyde vibration
1745 cm^{-1}	C = C stretching vibration
1635 cm^{-1}	azo bond (–N = N–)
1528 cm^{-1}	N–H stretching vibration
1492 cm^{-1}	C = C aromatic skeletal vibrations
1260 cm^{-1}	C–N stretching vibration
1186 cm^{-1}	C–OH stretching vibration
1045 cm^{-1}	C–OH stretching vibration
1028 cm^{-1}	Benzene mode coupling with stretching vibration of $–SO_3$
804 cm^{-1}	$–CH_3$ skeletal vibration
616 cm^{-1}	Sulfonic group

Table 3. List of some nanoreductives used in the removal of RB5 organic pollutants compared with the Mn–Ni powders used in the present work.

Alloy Name	Route of Synthesis	RB5 Concentration	Alloy Dose	Time	Removal	Ref.
Zero-valent iron powder	Commercial	100 mg/L	0.5g/L	120 min	100%	[56]
Mn–Al	Ball-milled	40 mg/L	2.5 g/L	20 min	100%	[35]
Ca–Al	Ball-milled	40 mg/L	1g/L	1 min	100%	[36]
FeSiB	Ball-milled	40mg/L	2.5 g/L	3 min	100%	[65]
MnAlFe	Ball-milled	40mg/L	2.5 g/L	5 min	100%	[29]
MnAlCo	Ball-milled	40mg/L	2.5 g/L	3 min	100%	[29]
Mn-30%Ni	Ball-milled	40mg/L	2.5 g/L	17 h	100%	[Present work]
Mn-20%Ni	Ball-milled	40mg/L	2.5 g/L	15 h	100%	[Present work]

4. Conclusions

In the current work, melt-spinning followed by high-energy ball-milling was successfully used to synthesize Mn-30at%Ni and Mn-20at%Ni powders. Through the use of several analysis techniques, including XRD, SEM-EDX, UV-visible, and FTIR, the efficiency and kinetics of the degrading response of these two alloys in the decolorization reaction of an aqueous solution of Reactive Black 5 were studied. Both particles displayed exceptional performance as decolorizing powders of Reactive Black 5 azo dye aqueous solution, despite the differences in chemical composition and crystalline size. The powdered Mn-20at%Ni particles exhibit good degrading efficiency and demonstrate a faster rate of reaction than the Mn-30at%Ni alloy. The valence electron arrangement explains this remarkable efficiency. When reducing Ni content, it promotes a higher number of reacting sites in the d-band. Later, this enhances electron transport between Mn and H^+, hastening the decolorization of RB5 solution containing powdered Mn-20at%Ni particles. Additionally, Mn-20at%Ni has the highest specific surface area (0.45 m^2 g^{-1}), which helps to account for the disparity in their decolorization effectiveness. The FTIR spectrum investigation shows an oxidative dissociation of the –N = N– bond, which promotes the presence of amines. The usage of Mn-Ni particle powders in industrial operations must be supplemented with an additional amine adsorption procedure, because these amines are also water pollutants. Chemical processes of decolorization in acidic and basic media are effectively proposed on the basis of all experimental findings linking the degradation process to redox reactions in acidic and alkaline solutions.

Author Contributions: Conceptualization, W.B.M. and M.A.H.; formal analysis, L.E. and B.H.; data curation, W.B.M., M.A.H. and M.K.; writing—original draft preparation, M.K., L.E. and J.-J.S.; writing—review and editing, M.K., B.H. and J.-J.S.; supervision. All authors have read and agreed to the published version of the manuscript.

Funding: This research received no external funding.

Institutional Review Board Statement: It is not necessary. This research does not involve humans or animals.

Informed Consent Statement: It is not mandatory/necessary in this research.

Data Availability Statement: Data may be requested from the authors.

Conflicts of Interest: The authors declare no conflict of interest.

References

1. Amin, N.K. Removal of direct blue-106 dye from aqueous solution using new activated carbons developed from pomegranate peel: Adsorption equilibrium and kinetics. *J. Hazard. Mater.* **2009**, *165*, 52–62. [CrossRef]
2. Yahagi, T.; Degawa, M.; Seino, Y.; Matsushima, T.; Nagao, M.; Sugimura, T.; Hashimoto, Y. Mutagenicity of carcinogenic azo dyes and their derivatives. *Cancer Lett.* **1975**, *1*, 91–96. [CrossRef] [PubMed]
3. Saratale, R.G.; Saratale, G.D.; Chang, J.S.; Govindwar, S.P. Bacterial decolorization and degradation of azo dyes: A review. *J. Taiwan Inst. Chem. Eng.* **2011**, *42*, 138–157. [CrossRef]

4. Çatalkaya, E.Ç.; Bali, U.; Şengül, F. Photochemical degradation and mineralization of 4-chlorophenol. *Environ. Sci. Pollut. Res.* **2003**, *10*, 113–120. [CrossRef] [PubMed]
5. Fu, W.; Yang, H.; Chang, L.; Hari-Bala; Li, M.; Zou, G. Anatase TiO_2 nanolayer coating on strontium ferrite nanoparticles for magnetic photocatalyst. *Colloids Surf. A Physico-Chem. Eng. Asp.* **2006**, *289*, 47–52. [CrossRef]
6. Asghar, A.; Raman, A.A.A.; Daud, W.M.A.W. Advanced oxidation processes for in-situ production of hydrogen peroxide/hydroxyl radical for textile wastewater treatment: A review. *J. Clean. Prod.* **2015**, *87*, 826–838. [CrossRef]
7. Khan, T.A.; Dahiya, S.; Ali, I. Use of kaolinite as adsorbent: Equilibrium, dynamics and thermodynamic studies on the adsorption of Rhodamine B from aqueous solution. *Appl. Clay Sci.* **2012**, *69*, 58–66. [CrossRef]
8. Tseng, W.J.; Lin, R.D. $BiFeO_3/\alpha$-Fe_2O_3 core/shell composite particles for fast and selective removal of methyl orange dye in water. *J. Colloid Interface Sci.* **2014**, *428*, 95–100. [CrossRef]
9. Qin, X.D.; Zhu, Z.W.; Liu, G.; Fu, H.M.; Zhang, H.W.; Wang, A.M.; Li, H.; Zhang, H.F. Ultrafast degradation of azo dyes catalyzed by cobalt-based metallic glass. *Sci. Rep.* **2016**, *5*, 18226. [CrossRef]
10. Chen, S.S.; Hsu, H.D.; Li, C.W. A new method to produce nanoscale iron for nitrate removal. *J. Nanopart. Res.* **2004**, *6*, 639–647. [CrossRef]
11. Fan, J.; Guo, Y.H.; Wang, J.J.; Fan, M.H. Rapid Decolorization of azo Dye Methyl Orange in Aqueous Solution by Nanoscale zerovalent Iron Particles. *J. Hazard. Mater.* **2009**, *166*, 904–910. [CrossRef]
12. Kumar, M.; Chakraborty, S. Chemical denitrification of water by zero-valent magnesium powder. *J. Hazard. Mater.* **2006**, *135*, 112–121. [CrossRef]
13. Noubactep, C. Elemental metals for environmental remediation: Learning from cementation process. *J. Hazard. Mater.* **2010**, *181*, 1170–1174. [CrossRef]
14. Kanel, S.R.; Manning, B.; Charlet, L.; Choi, H. Removal of arsenic(III) from groundwater by nanoscale zero-valent iron. *Environ. Sci. Technol.* **2005**, *39*, 1291–1298. [CrossRef]
15. Schrick, B.; Blough, J.L.; Jones, A.D.; Mallouk, T.E. Hydrodechlorination of trichloroethylene to hydrocarbons using bimetallic nickel-iron nanoparticles. *Chem. Mater.* **2002**, *14*, 5140–5147. [CrossRef]
16. Chang, J.H.; Cheng, S.F. The remediation performance of a specific electrokinetics integrated with zero-valent metals for perchloroethylene contaminated soils. *J. Hazard. Mater.* **2006**, *131*, 153–162. [CrossRef] [PubMed]
17. Xiong, Z.; Zhao, D.; Pan, G. Rapid and complete destruction of perchlorate in water and ion-exchange brine using stabilized zero-valent iron nanoparticles. *Water Res.* **2007**, *41*, 3497–3505. [CrossRef] [PubMed]
18. Hu, J.; Lo, I.M.C.; Chen, G. Fast removal and recovery of Cr(VI) using surface-modified jacobsite ($MnFe_2O_4$) nanoparticles. *Langmuir* **2005**, *21*, 11173–11179. [CrossRef]
19. Dutta, A.K.; Maji, S.K.; Adhikary, B. γ-Fe2O3 Nanoparticles: An Easily Recoverable Effective Photo-Catalyst for the Degradation of Rose Bengal and Methylene Blue Dyes in the Waste-Water Treatment Plant. *Mater. Res. Bull.* **2014**, *49*, 28–34. [CrossRef]
20. Huang, Y.; Fan, W.; Long, B.; Li, H.; Zhao, F.; Liu, Z.; Tong, Y.; Ji, H. Visible Light $Bi_2S_3/Bi_2O_3/Bi_2O_2CO_3$ Photocatalyst for Effective Degradation of Organic Pollutions. *Appl. Catal. B Environ.* **2016**, *185*, 68–76. [CrossRef]
21. Low, J.; Yu, J.; Jaroniec, M.; Wageh, S.; Al-Ghamdi, A.A. Heterojunction Photocatalysts. *Adv. Mater.* **2017**, *29*, 1601694. [CrossRef] [PubMed]
22. Kurian, M.; Nair, D.S. Heterogeneous Fenton Behavior of Nano Nickel Zinc Ferrite Catalysts in the Degradation of 4-Chlorophenol from Water under Neutral Conditions. *J. Water Process Eng.* **2015**, *8*, e37–e49. [CrossRef]
23. Ma, H.; Wang, H.; Na, C. Microwave-Assisted Optimization of Platinum-Nickel Nanoalloys for Catalytic Water Treatment. *Appl. Catal. B Environ.* **2015**, *163*, 198–204. [CrossRef]
24. Chaturvedi, S.; Dave, P.N.; Shah, N.K. Applications of Nano-Catalyst in New Era. *J. Saudi Chem. Soc.* **2012**, *16*, 307–325. [CrossRef]
25. Lin, S.T.; Thirumavalavan, M.; Jiang, T.Y.; Lee, J.F. Synthesis of ZnO/Zn Nano Photocatalyst Using Modified Polysaccharides for Photodegradation of Dyes. *Carbohydr. Polym.* **2014**, *105*, 1–9. [CrossRef]
26. Adeleye, A.S.; Conway, J.R.; Garner, K.; Huang, Y.; Su, Y.; Keller, A.A. Engineered Nanomaterials for Water Treatment and Remediation: Costs, Benefits, and Applicability. *Chem. Eng. J.* **2016**, *286*, 640–662. [CrossRef]
27. Anjum, M.; Miandad, R.; Waqas, M.; Gehany, F.; Barakat, M.A. Remediation of Wastewater Using Various Nano-Materials. *Arab. J. Chem.* **2019**, *12*, 4897–4919. [CrossRef]
28. Akhavan, O. Lasting Antibacterial Activities of Ag-TiO_2/Ag/a-TiO_2 Nanocomposite Thin Film Photocatalysts under Solar Light Irradiation. *J. Colloid Interface Sci.* **2009**, *336*, 117–124. [CrossRef]
29. Mbarek, W.; Saurina, J.; Escoda, L.; Pineda, E.; Khitouni, M.; Suñol, J.J. Effects of the Addition of Fe, Co on the Azo Dye Degradation Ability of Mn-Al Mechanically Alloyed Powders. *Metals* **2020**, *10*, 1578. [CrossRef]
30. AboliGhasemabadi, M.; Mbarek, W.B.; Cerrillo-Gil, A.; Roca-Bisbe, H.; Casabella, O.; Blanquez, P.; Pineda, E.; Escoda, L.; Sunol, J.J. Azo-dye degradation by Mn–Al powders. *J. Environ. Manag.* **2020**, *258*, 110012. [CrossRef]
31. Wang, J.Q.; Liu, Y.H.; Chen, M.W.; Xie, G.Q.; Louzguine-Luzgin, D.V.; Inoue, A.; Perepezko, J.H. Rapid Degradation of Azo Dye by Fe-Based Metallic Glass Powder. *Adv. Funct. Mater.* **2012**, *22*, 2567–2570. [CrossRef]
32. Wang, J.Q.; Liu, Y.H.; Chen, M.W.; Louzguine-Luzgin, D.V.; Inoue, A.; Perepezko, J.H. Excellent capability in degrading azo dyes by MgZn-based metallic glass powders. *Sci. Rep.* **2012**, *2*, 418. [CrossRef] [PubMed]
33. Sapkota, B.B.; Mishra, S.R. A Simple Ball Milling Method for the Preparation of p-CuO/n-ZnO Nanocomposite Photocatalysts with High Photocatalytic Activity. *J. Nanosci. Nanotechnol.* **2013**, *13*, 6588–6596. [CrossRef]

34. Suryanarayana, C. Mechanical alloying and milling. *Prog. Mater. Sci.* **2001**, *46*, 1–184. [CrossRef]
35. Ben Mbarek, W.; Azabou, M.; Pineda, E.; Fiol, N.; Escoda, L.; Sunol, J.J.; Khitouni, M. Rapid degradation of azo-dye using Mn–Al powders produced by ball-milling. *RSC Adv.* **2017**, *7*, 12620–12628. [CrossRef]
36. Ben Mbarek, W.; Pineda, E.; Fiol, N.; Escoda, L.; Sunol, J.J.; Khitouni, M. High efficiency decolorization of azo dye Reactive Black 5 by Ca-Al particles. *J. Environ. Chem. Eng.* **2017**, *5*, 6107–6113. [CrossRef]
37. Ghasemabadi, M.A.; Mbarek WBen Casabella, O.; Roca-Bisbe, H.; Pineda, E.; Escoda, L.; Sunol, J.J. Application of mechanically alloyed MnAl particles to de-colorization of azo dyes. *J. Alloys Comp.* **2018**, *741*, 240–245. [CrossRef]
38. Kuyama, J.; Inui, H.; Imaoka, S.; Ishihara, K.N.; Shinhu, P. Nanometer-sized crystals formed by the mechanical alloying in the Ag-Fe system. *Jpn. J. Appl. Phys.* **1991**, *30*, L854. [CrossRef]
39. Kuschke, W.M.; Keller, R.M.; Grahle, P.; Mason, R.; Arzt, E. Mechanisms of powder milling investigated by X-ray diffraction and quantitative metallography. *Int. J. Mater. Res.* **1995**, *86*, 804–813. [CrossRef]
40. Mhadhbi, M.; Khitouni, M.; Azabou, M.; Kolsi, A. Characterization of Al and Fe nanosized powders synthesized by high energy mechanical milling. *J. Mater. Charact.* **2008**, *59*, 944–950. [CrossRef]
41. El-Eskandarany, M.S. *Mechanical Alloying for Fabrication of Advanced Engineering Materials*; Noyes Publications/William Andrew Publishing: Norwich, NY, USA, 2001.
42. Suryanarayana, C.; Koch, C.C. *Non-Equilibrium Processing of Materials*; Suryanarayana, C., Ed.; Pergamon: New York, NY, USA, 1999; pp. 313–344.
43. Cao, J.; Wei, L.; Huang, Q.; Wang, L.; Han, S. Reducing degradation of azo dye by zero-valent iron in aqueous solution. *Chemosphere* **1999**, *38*, 565–571. [CrossRef]
44. Nam, S.; Tratnyek, P.G. Reduction of azo dyes with zero-valent iron. *Water Res.* **2000**, *34*, 1837–1845. [CrossRef]
45. Wu, F.; Deng, N.; Hua, H. Degradation mechanism of azo dye C. I. reactive red 2 by iron powder reduction and photooxidation in aqueous solutions. *Chemosphere* **2000**, *4*, 1233–1238. [CrossRef]
46. Stylidi, M.; Kondarides, D.I.; Verykios, X.E. Pathways of solar light-induced photocatalytic degradation of azo dyes in aqueous TiO2 suspensions. *Appl. Catal. B* **2003**, *40*, 271–286. [CrossRef]
47. Pauling, L. The nature of the interatomic forces in metals. *Phys. Rev.* **1938**, *54*, 899–904. [CrossRef]
48. Pauling, L. A resonating-valence-bond theory of metals and intermetallic compounds. *Proc. R. Soc. London. Ser. A Math. Phys. Sci.* **1949**, *196*, 343–362. [CrossRef]
49. Dowden, D.A. Heterogeneous catalysis. Part I. Theoretical basis. *J. Chem. Soc.* **1950**, *56*, 242–265. [CrossRef]
50. Zhang CZhu ZZhang, H.; Sun, Q.; Liu, K. Effects of cobalt content on the decolorization properties of Fe-Si-B amorphous alloys. *Results Phys.* **2018**, *10*, 1–4. [CrossRef]
51. Ponder, S.M.; Darab, J.G.; Mallouk, T.E. Remediation of Cr(VI) and Pb(II) aqueous solutions using supported, nanoscale zero-valent iron. *Environ. Sci. Technol.* **2000**, *34*, 2564–2569. [CrossRef]
52. Deng, J.; Feng, S.; Ma, X.; Tan, C.; Wang, H.; Zhou, S.; Zhang, T.; Li, J. Heterogeneous degradation of Orange II with peroxymonosulfate activated by ordered mesoporous $MnFe_2O_4$. *Separ. Purif. Technol.* **2016**, *167*, 181–189. [CrossRef]
53. Chen, J.X.; Zhu, L.Z. Heterogeneous UV-Fenton catalytic degradation of dyestuff in water with hydroxyl-Fe pillared bentonite. *Catal. Today* **2007**, *126*, 463–470. [CrossRef]
54. Luo, X.K.; Li, R.; Huang, L.; Zhang, T. Nucleation and growth of nanoporous copper ligaments during electrochemical dealloying of Mg-based metallic glasses. *Corros. Sci.* **2013**, *67*, 100–108. [CrossRef]
55. Yang, Y.Y.; Li, Z.L.; Wang, G.; Zhao, X.P.; Crowley, D.E.; Zhao, Y.H. Computational identification and analysis of the key biosorbent characteristics for the biosorption process of Reactive Black 5 onto fungal biomass. *PLoS ONE* **2012**, *7*, e33551. [CrossRef] [PubMed]
56. Satapanajaru, T.; Chompuchan, C.; Suntornchot, P.; Pengthamkeerati, P. Enhancing Decolorization of Reactive Black 5 and Reactive Red 198 during Nano Zerovalent Iron Treatment. *Desalination* **2011**, *266*, 218–230. [CrossRef]
57. Zhang, C.Q.; Zhu, Z.W.; Zhang, H.F.; Hu, Z.Q. Rapid decolorization of Acid Orange II aqueous solution by amorphous zero-valent iron. *J. Environ. Sci.* **2012**, *24*, 1021–1026. [CrossRef] [PubMed]
58. Zhang, L.; Gao, X.; Zhang, Z.; Zhang, M.; Cheng, Y.; Su, J. A doping lattice of aluminum and copper with accelerated electron transfer process and enhanced reductive degradation performance. *Sci. Rep.* **2016**, *6*, 31797. [CrossRef]
59. Mbarek, W.B.; Escoda, L.; Saurina, J.; Pineda, E.; Alminderej, F.M.; Khitouni, M.; Suñol, J.J. Nanomaterials as a Sustainable Choice for Treating Wastewater: A Review. *Materials* **2022**, *15*, 8576. [CrossRef]
60. Méndez-Martínez, A.J.; Dávila-Jiménez, M.M.; Ornelas-Dávila, O.; Elizalde-González, M.P.; Arroyo-Abad, U.; Sirés, I.; Brillas, E. Electrochemical reduction and oxidation pathways for Reactive Black 5 dye using nickel electrodes in divided and undivided cells. *Electrochim. Acta* **2012**, *59*, 140–149. [CrossRef]
61. Almeida, E.J.R.; Corso, C.R. Comparative study of toxicity of azo dye Procion Red MX-5B following biosorption and biodegradation treatments with the fungi *Aspergillus niger* and *Aspergillus terreus*. *Chemosphere* **2014**, *112*, 317–322. [CrossRef]
62. Shilpa, S.; Shikha, R. Biodegradation of Dye Reactive Black-5 by a Novel Bacterial Endophyte. *Int. Res. J. Environ. Sci.* **2015**, *4*, 44–53.
63. El Bouraie, M.; SalahEdin, W. Biodegradation of Reactive Black 5 by *Aeromonas hydrophila* strain isolated from dye contaminated textile wastewater. *Sustain. Environ. Res.* **2016**, *26*, 209–216. [CrossRef]

64. Elías, V.R.; Sabre, E.V.; Winkler, E.L.; Satuf, M.L.; Rodriguez-Castellón, E.; Casuscelli, S.G.; Eimer, G.A. Chromium and titanium/chromium-containing MCM-41 mesoporous silicates as promising catalysts for the photobleaching of azo dyes in aqueous suspensions. A multitechnique investigation. *Microporous Mesoporous Mater.* **2012**, *163*, 85–95. [CrossRef]
65. Ben Mbarek, W.; Daza, J.; Escoda, L.; Fiol, N.; Pineda, P.; Khitouni, M.; Suñol, J.J. Removal of Reactive Black 5 Azo Dye from Aqueous Solutions by a Combination of Reduction and Natural Adsorbents Processes. *Metals* **2023**, *13*, 474. [CrossRef]